

## RESEARCH ARTICLE

# Residual stress versus microstructural effects on the strength and toughness of phase-separated PbO–B<sub>2</sub>O<sub>3</sub>–Al<sub>2</sub>O<sub>3</sub> glasses

Gisele G. Santos<sup>1</sup>  | Oscar Peitl<sup>1</sup> | Akio Koike<sup>2</sup> | Shusaku Akiba<sup>2</sup> |  
Shigeki Sawamura<sup>2</sup> | Mikio Nagano<sup>2</sup> | Yoshitaka Saijo<sup>3</sup> | Susumu Harako<sup>3</sup> |  
Satoshi Yoshida<sup>2</sup>  | Edgar D. Zanotto<sup>1</sup> 

<sup>1</sup>Department of Materials Engineering,  
Federal University of São Carlos, São  
Carlos, SP, Brazil

<sup>2</sup>Materials Integration Laboratories, AGC  
Inc., Yokohama, Japan

<sup>3</sup>Innovative Technology Laboratories,  
ACG Inc., Yokohama, Japan

**Correspondence**

Gisele G. Santos, Department of Materials  
Engineering, Federal University of São  
Carlos, São Carlos, SP, Brazil.  
Email: giseleagu@gmail.com

**Funding information**

Fundação de Amparo à Pesquisa do  
Estado de São Paulo, Grant/Award  
Number: 2013/07793-6

**Abstract**

A few authors have reasonably proposed that liquid–liquid phase-separated (LLPS) glasses could show improved fracture strength,  $S_f$ , and toughness,  $K_{Ic}$ , as the second phase could provide a barrier to crack propagation via deflection, bowing, trapping, or bridging. Due to the associated tensile or compressive residual stresses, the second phase could also act as a toughening or a weakening mechanism. In this work, we investigated five glasses of the PbO–B<sub>2</sub>O<sub>3</sub>–Al<sub>2</sub>O<sub>3</sub> system spanning across the miscibility gap: Four of them undergo LLPS—three are binodal (two B<sub>2</sub>O<sub>3</sub>-rich and one PbO-rich) and one is spinodal—and one does not show LLPS (composition outside the miscibility gap). Their compositions were designed in such a way that the amorphous particles are under compressive residual stresses in some and under tensile residual stresses in others. The following mechanical properties were determined: the Vickers hardness, ball on three balls (B3B) strength, and toughness,  $K_{Ic-SEVNB}$  (single-edge V-notch beam [SEVNB]). The microstructures and compositions were analyzed using scanning electron microscopy with energy-dispersive X-ray spectrometry. The spinodal glass showed, by far, the best mechanical properties. Its  $K_{Ic-SEVNB} = 1.6 \pm 0.1 \text{ MPa m}^{1/2}$ , which embodies an increase of almost 50% over the B<sub>2</sub>O<sub>3</sub>-rich binodal composition, and 90% considering the PbO-rich binodal composition. Moreover, its fracture strength,  $S_f = 166 \pm 7 \text{ MPa}$ , is one of the highest ones ever reported for an LLPS glass. Fracture analyses evidenced that the spinodal composition exhibited the lowest net stress at the fracture point. Moreover, calculations indicate that the internal residual stress level is the lowest in the spinodal glass. The overall results indicate that the *microstructural effect* of the spinodal glass is the most significant factor for its superior mechanical properties. This work corroborates the idea that LLPS provides a feasible and stimulating solution to improve the mechanical properties of glasses.

**KEYWORDS**

glass, mechanical properties, microstructure, phase separation

## 1 | INTRODUCTION

Immiscibility in glass-forming liquids is a phenomenon that can be understood through the thermodynamics of mixing.<sup>1</sup> For some compositions, the system is more stable if the supercooled liquid (SCL) components segregate into two or more liquid phases. The region in a phase diagram where this phenomenon occurs is called *miscibility gap* or *immiscibility dome*. Inside the miscibility gap, there is a binodal region where the typical morphology of the minor phase is droplet-like, whereas compositions in the central region of the dome, referring to spinodal decomposition, usually exhibit a snakelike interconnected nano- or microstructure. Explanations and in-depth discussions about liquid immiscibility in glass-formers can be found in several books and review papers.<sup>1–4</sup>

Glasses showing liquid–liquid phase separation (LLPS) at nanoscale could be transparent to visible light; however, when the second phase has micron-sized particles and, in this case, a widely different refractive index compared with that of the matrix (lead-rich vs. lead-poor phases), they are normally opaque or translucent because of light scattering. These glasses have found some commercial applications, such as the famous Vycor glass, porous substrates (after leaching out one phase),<sup>2</sup> perfume flasks, and cooking ware.<sup>5</sup> Interestingly, some LLPS glasses show improved mechanical properties, which is of enormous interest in the glass field, and in some cases, they might even be transparent.

This discussion is not new, and the literature brings several studies on the mechanical properties of oxide glasses showing LLPS, such as the  $\text{Li}_2\text{O}-\text{B}_2\text{O}_3-\text{SiO}_2$ ,<sup>6</sup>  $\text{Na}_2\text{O}-\text{B}_2\text{O}_3-\text{SiO}_2$ ,<sup>6–8</sup>  $\text{Na}_2\text{O}-\text{CaO}-\text{SiO}_2$ ,<sup>9</sup>  $\text{B}_2\text{O}_3-\text{SiO}_2$ ,<sup>9,10</sup>  $\text{PbO}-\text{B}_2\text{O}_3$ ,<sup>11–13</sup>  $\text{K}_2\text{O}-\text{Li}_2\text{O}-\text{SiO}_2$ ,<sup>14</sup> and  $\text{B}_2\text{O}_3-\text{SiO}_2-\text{Al}_2\text{O}_3-\text{P}_2\text{O}_5$ <sup>15</sup> glasses. Recently, these studies have resurfaced in the field of computer simulations to predict the mechanical properties of phase-separated glasses.<sup>16,17</sup> Some selected previous studies addressing the mechanical properties of LLPS systems are briefly summarized as follows.

Seal et al.<sup>7</sup> studied the effect of phase separation on the fracture toughness of an  $\text{SiO}_2-\text{B}_2\text{O}_3-\text{Na}_2\text{O}$  glass using four compositions inside the miscibility gap (10-wt%  $\text{Na}_2\text{O}-70$ -wt%  $\text{B}_2\text{O}_3-20$ -wt%  $\text{SiO}_2$ , 10-wt%  $\text{Na}_2\text{O}-60$ -wt%  $\text{B}_2\text{O}_3-30$ -wt%  $\text{SiO}_2$ , 10-wt%  $\text{Na}_2\text{O}-40$ -wt%  $\text{B}_2\text{O}_3-50$ -wt%  $\text{SiO}_2$ , and 10-wt%  $\text{Na}_2\text{O}-30$ -wt%  $\text{B}_2\text{O}_3-60$ -wt%  $\text{SiO}_2$ ), with the last one being inside the spinodal region. They found  $K_{Ic}$  values ranging from 1.4 to 1.5  $\text{MPa m}^{1/2}$ —the highest ones for the spinodal composition—after thermal treatments at 650°C/16 h and 600°C/64 h, respectively. Considering that the fracture toughness of a common single-phase sodium borosilicate glass is 0.7–0.8  $\text{MPa m}^{1/2}$ , this is a

very significant increase. Those authors attributed the best performance of the spinodal glass to the high interconnectivity of the liquid phases, which provides a barrier to crack propagation.

Mecholsky<sup>18</sup> reported a 30% increase in the fracture toughness of a homogeneous glass in a phase-separated alkali–borosilicate system, reaching 1.1  $\text{MPa m}^{1/2}$ ; however, the author did not discuss the relationship between fracture toughness and the binodal or spinodal microstructure. According to Mecholsky, the best correlation parameter for the toughness increase was the surface area to volume ratio of the inclusions. The study showed that  $K_{Ic}$  reached a maximum when this ratio was  $\sim 8-10 \mu\text{m}^2/\mu\text{m}^3$ .

Häßler and Rüssel<sup>8</sup> studied the mechanical properties of  $\text{SiO}_2-\text{B}_2\text{O}_3-\text{Na}_2\text{O}$  ternary LLPS glasses containing 60-mol%  $\text{SiO}_2-37$ -mol%  $\text{B}_2\text{O}_3-3$ -mol%  $\text{Na}_2\text{O}$  treated at temperatures ranging from 500 to 680°C for 1–80 h to develop a phase-separated microstructure consisting of droplets rich in  $\text{Na}_2\text{O}$  and  $\text{B}_2\text{O}_3$  ( $CTE = 6.5-8.5 \times 10^{-6} \text{ K}^{-1}$ ) and an  $\text{SiO}_2$ -rich matrix phase ( $CTE = 3.0-4.0 \times 10^{-6} \text{ K}^{-1}$ ). Interestingly, these LLPS glasses were *transparent* as a result of their small particle size, which ranged from 20 to 50 nm in samples treated at 540°C for 5 h and from 80 to 400 nm in those treated at 680°C for 80 h. The Vickers hardness and elastic modulus did not change within the measurement errors, but the bending strength showed a maximum for particle sizes around 70 nm (115 MPa) and 99–115 MPa for thermal treatments at 600, 620, and 640°C for 20 h. Very large (120–160 nm) or very small (30–50 nm) droplet diameters lead to significantly lower bending strength values. Additionally, the conditions that generated samples with the highest bending strength exhibited an intermediate value of  $\Delta CTE$  ( $3.8-4.1 \times 10^{-6} \text{ K}^{-1}$ ). Those authors attributed this increase in bending strength to *residual stresses* formed during cooling, as the matrix formed mostly by  $\text{SiO}_2$  has a lower CTE and a higher  $T_g$  than the droplet phase, which is rich in  $\text{Na}_2\text{O}$  and  $\text{B}_2\text{O}_3$ . Thus, the generated stress cannot relax at temperatures below the lowest  $T_g$ .

Tang et al.<sup>16</sup> used peridynamic simulations to investigate the effect of nanoscale liquid phase separation on the crack propagation mechanism of a calcium aluminosilicate glass. The simulation was based on a previous study by Martel et al.<sup>19</sup> The diameter of the nano-inclusions was fixed at 200 nm, and their volume fraction was fixed at 30%; the spinodal composition was excluded. Those authors carried out some simulations varying the ratio between the elastic modulus of the particle and the matrix ( $E_i/E_m = 0.5, 1.0, \text{ and } 2.0$ ) and investigated the effect of strain rate, stiffness, and fracture surface energy of the nano-inclusions on the nature of the toughening mechanisms. The study led to very interesting observations, but the most

curious one refers to stiffness. Those authors noticed that the overall stiffness (the slope of the stress–strain curve) of the phase-separated glasses increases with increasing the elastic modulus of the nano-inclusions, as expected ( $E_i/E_m = 2.0 > E_i/E_m = 1.0 > E_i/E_m = 0.5$ ), but softer inclusions result in an increase in the ultimate strain before fracture. This is because soft particles locally reduce the stress experienced by the glass and, therefore, delay yielding. They concluded that, in most cases, LLPS can lead to increased glass fracture energy, and that the toughening mechanism is due to a balance among propensity to crack deflection, cohesion of the phases, plastic energy dissipation and, to a lower extent, to crack surface roughness. The best results regarding toughening were found when soft, yet tough, nano-inclusions were the second phase.

The phase diagram and phase separation limits of the PbO–B<sub>2</sub>O<sub>3</sub> system have been extensively studied over time.<sup>20–23</sup> For binodal compositions, the LLPS microstructure consists of spherical particles of one phase embedded in a continuous matrix of the second phase.<sup>24,25</sup> The literature brings some works addressing the mechanical properties of glasses of this system.<sup>11–13,25</sup> According to these studies, the fracture toughness of compositions with a B-rich matrix is around 0.8–0.9 MPa m<sup>1/2</sup>. The fracture toughness peaks at ~1.6 MPa m<sup>1/2</sup> and the fracture energy maximize (37.6 J/m<sup>2</sup>)<sup>12</sup> for glasses with ~32-wt% PbO.<sup>12,13</sup> The elastic modulus increases as the PbO amount increases, being 44.5 GPa for a glass containing 40-wt% PbO,<sup>25</sup> whereas the flexural strength is highest for glasses with 13-wt% PbO (106 MPa) and 35-wt% PbO (102 MPa).<sup>12</sup> Residual stresses are said to potentially affect the mechanical properties of these glasses,<sup>12</sup> but they were not measured.

As previously shown, to the best of our knowledge, there are few results on the mechanical properties of glasses with spinodal type microstructures. Moreover, the effect of internal residual stress (due to the thermal and elastic mismatch between the two phases) has been scarcely explored, and its relevance to the improvement of mechanical properties is still elusive.

In this work, we analyzed glasses of the PbO–B<sub>2</sub>O<sub>3</sub>–Al<sub>2</sub>O<sub>3</sub> system using the Vickers hardness,  $H_v$ , flexural strength,  $S_f$  (ball on three balls tests), and critical stress intensity factor,  $K_{Ic}$ , measured following the ISO 23146 standard (Test methods for fracture toughness of monolithic ceramics—single-edge V-notch beam [SEVNB] method)<sup>26</sup> for binodal and spinodal glass compositions. In addition to the expected *microstructural* effects (e.g., binodal vs. spinodal microstructures), the *internal residual stresses* might also play an important role. Here, we measure, compare, and discuss the mechanical properties of phase-separated glasses in light of current knowledge about the effect of residual stresses.

**TABLE 1** Nominal glass compositions prepared and studied in this work (in wt%)

Compositions	PbO	B <sub>2</sub> O <sub>3</sub>	Al <sub>2</sub> O <sub>3</sub>
Binodal-1' (B1')	2.0	91.0	7.0
Binodal-1 (B1)	7.7	85.3	7.0
Spinodal	14.6	78.4	7.0
Binodal-2 (B2)	26.1	66.9	7.0
Outside the gap (OTG)	34.6	58.4	7.0

## 2 | EXPERIMENTAL PROCEDURES

At first, we needed to choose compositions under the immiscibility dome of an adequate system showing LLPS, for which we chose the PbO–B<sub>2</sub>O<sub>3</sub> because of the possibility of controlling the LLPS microstructure. However, the exact miscibility limits for this system are uncertain<sup>20,21,27</sup>; thus, parts of our initial composition choices were made based on previous works, whereas other compositions were empirically chosen based on our own preliminary results. The strategy was to produce five glasses: one in the central spinodal region of the miscibility gap, two in the binodal region rich in B<sub>2</sub>O<sub>3</sub> (binodal-1 = B1 and binodal-1' = B1'), one in the binodal region rich in PbO (binodal-2 = B2), and one even richer in PbO outside the miscibility gap (OTG). These compositions were designed in such a way that the amorphous particles are under *compressive* residual stresses in B1 and B1' and under *tensile* stresses in B2. At first, the idea behind the B1' composition was to obtain a B<sub>2</sub>O<sub>3</sub>-rich glass outside the miscibility gap, mirroring the OTG composition, but on the other side of the gap; however, the B1' glass also exhibited LLPS on cooling.

The spinodal composition is similar to the one previously studied by Craievich in a small angle X-ray scattering work.<sup>28</sup> The addition of 7-wt% Al<sub>2</sub>O<sub>3</sub> was intended to decrease the critical temperature<sup>28</sup> and the hygroscopicity of these glasses, so that especially the glasses with high B<sub>2</sub>O<sub>3</sub> content became less prone to chemical attack than trial glasses containing less alumina. Previous studies adding 5-wt% Al<sub>2</sub>O<sub>3</sub> showed that the lead–borate LLPS behavior does not change in the spinodal composition.<sup>29</sup> The final nominal compositions are shown in Table 1 and Figure 1, which illustrate their approximate location in the phase diagram. The binodal-2' composition, B2' (7-wt% Al<sub>2</sub>O<sub>3</sub>–30-wt% PbO–63-wt% B<sub>2</sub>O<sub>3</sub>) in Figure 1, was only a test composition; it served to show the LLPS limits, but no further work was conducted with it.

The starting chemicals were H<sub>3</sub>BO<sub>3</sub> (Sigma-Aldrich, ≥99.8%), Pb<sub>3</sub>O<sub>4</sub> (Alfa Aesar, 97%), and Al<sub>2</sub>O<sub>3</sub> (APC-G, Alcoa). They readily react and melt on heating. Previous experiments in our laboratory showed that Pb<sub>3</sub>O<sub>4</sub>

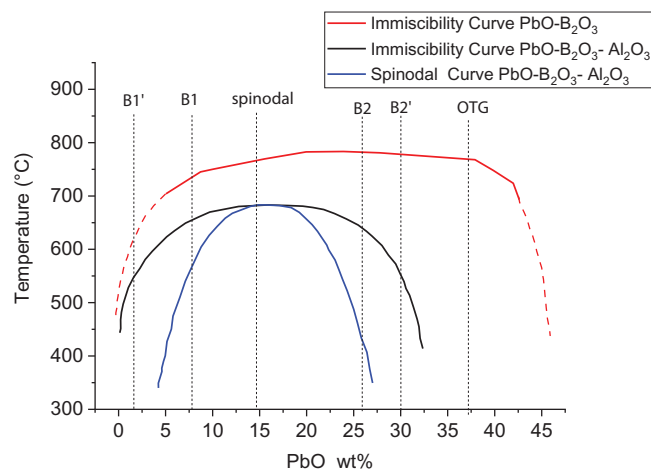


**FIGURE 1** Approximate immiscibility dome of the PbO–B<sub>2</sub>O<sub>3</sub> system without Al<sub>2</sub>O<sub>3</sub> (redline) and with 5-wt% Al<sub>2</sub>O<sub>3</sub> (black line). The redline was proposed by Podlesny et al.,<sup>27</sup> whereas the blue and black lines were traced following Zarzycki and Naudin.<sup>30</sup> The black gap is likely similar to the actual gap of this study. The glass compositions of the current work are indicated by vertical dashed lines.

decomposes and releases oxygen, creating an oxidative atmosphere that precludes Pb reduction to the metallic state, thus avoiding chemical reaction with the platinum crucible. Approximately 100 g of each composition was carefully weighted, well mixed, and homogenized in a jar mill (Solab) for 20 h.

The melting operation was conducted in a Deltech furnace at 1000–1100°C. All compositions were remelted at least twice to yield homogeneous glasses. The samples were poured into different brass molds depending on the future tests: 12 × 2.5-mm<sup>2</sup> small discs for ball on three balls (B3B) strength tests and 3.5 × 4.5 × 45 mm<sup>3</sup> bars for *K<sub>IC</sub>* tests.

Small (~20 mg) pieces of the glasses were evaluated by differential scanning calorimetry (DSC) (NETZSCH, DSC 404) to obtain the glass transition and crystallization temperatures. The DSC experiments were performed using a standard platinum pan, with a heating rate of 10°C/min up to 800–900°C. The glass samples were then submitted to annealing heat treatments (EDG, 3P-S) at 50°C below the DSC *T<sub>g</sub>* for 2 h followed by a cooling rate of 3°C/min.

Disc samples of the B1, spinodal, B2, and OTG compositions were ground using 150-mesh sandpaper in a polishing machine with isopropyl alcohol (to avoid chemical attack) to flatten both faces, and polishing was carried out sequentially using 220, 320, 400, 500, 600, and 1200-mesh sandpapers. Their structures and compositions were analyzed by scanning electron microscopy (SEM, Hitachi High-Tech SU8230) with energy-dispersive X-ray spectroscopy (EDS, Bruker XFlash 5060FQ) using a low voltage (4 kV). The

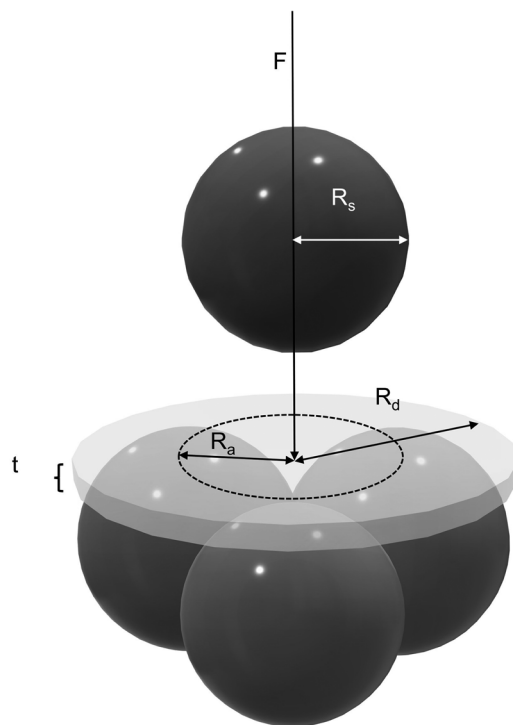


**FIGURE 2** Sample holder arrangement for calculations of the parameters in Equation (1). In our measurements,  $R_s = 5$  mm,  $R_d \sim 7$  mm, and  $t = 1.5$ –2 mm. Source: After Ref. [31]

fresh surfaces were obtained by fracturing the samples in a nitrogen-substituted glove box. The surfaces were coated with ~3-nm Pt film to avoid charge buildup. The resulting micrographs were analyzed using the Fiji ImageJ processing software with the trainable segmentation feature to estimate the average particle sizes and volume fraction.

For the B3B tests, 8–12 disc-shaped samples were prepared for each composition and heat-treatment condition: Not heat treated (only annealed at 50°C below *T<sub>g</sub>*) and heat treated at *T<sub>g</sub>* for 1 h in a homemade horizontal furnace, monitored with calibrated chromel–alumel thermocouples to evaluate the effect of heat treatments (which, in principle, caused further development of the LLPS process) on flexural strength. The next step included grinding and polishing: The glass discs were ground using 150-mesh sandpaper in an automatic polishing machine (Struers, LaboPol-30) at 200 rpm to flatten their surfaces. The finishing process was performed using a sequence of 220, 320, 400, and 500-mesh grit sandpapers on both sides.

Flexural strength was calculated as proposed by Börger et al.,<sup>31</sup> using the arrangement shown in Figure 2 and the following equation:

$$\sigma = \frac{F}{t^2} f \quad (1)$$

where  $F$  is the load (N),  $t$  is the plate thickness,  $f$  is a dimensionless factor that is affected by the following parameters: load used, contact radius,  $R_a$ , disc radius,  $R_d$ , disc thickness,  $t$ , and the elastic constants of the disc and the balls,  $E$  and  $\nu$ . Börger et al.<sup>31</sup> provided an extensive discussion about the calculation of  $f$ .

The fractured samples were analyzed by optical microscopy (OM) to estimate the mirror radius,  $R_m$ , or the fracture region close to the origin where the surface is still smooth. The residual stress at the point of fracture,  $\sigma_r$ , was calculated through the following equation (2)<sup>32</sup>:

$$\sigma_r = \frac{A}{\sqrt{R_m}} - \sigma_a \quad (2)$$

where  $A$  is a constant that depends on the material composition, with the same units as  $K_{Ic}$  (MPa m<sup>1/2</sup>), which can be obtained by measuring as many mirror regions as possible and relating them to the applied stress,  $\sigma_a$ . The slope of the  $\sigma_a$  versus  $1/\sqrt{R_m}$  line gives the constant  $A$ ,<sup>32</sup>  $R_m$  is the mirror radius (m), and  $\sigma_a$  is the applied fracture stress (MPa).

For the Vickers hardness tests, one disc-shaped sample of each composition was ground flat on both faces using 150-mesh sandpaper. After that, the samples were polished according to the process described previously but using additional sandpapers (600 and 1200 mesh). The samples were tested on a square-based diamond pyramid indenter using a 30-N load for 15 s. The number of indents was between 10 and 12, and the local humidity was 49%–51%. The diagonals of each indentation impression were measured, and the hardness was calculated through Equation (3). The schematic representation is shown in Figure 3.

$$H = 1.854 \frac{P}{d^2} \quad (3)$$

where  $P$  is the load used, and  $d$  is the average diagonal length of the impression. The indentation toughness obtained from the Vickers tests,  $K_{c-ind}$ , was calculated according to the  $l/a$  factor, that is, the crack length,  $l$ , divided by half of the diagonal of the Vickers indent,  $a$ . This value can be used to identify the type of crack generated by a Vickers indentation.<sup>33</sup> The indentation-induced cracks in the present samples ( $0.25 \leq l/a \leq 2.5$ ) can be classified as of the Palmqvist type, although these values varied widely, from 0.9 (BI' composition) to 2.4 (OTG composition). In this case, the following equation (4)<sup>33</sup> was used:

$$K_{c-ind} = 0.035 \left( \frac{l}{a} \right)^{-1/2} \left( \frac{H}{E\Phi} \right)^{-2/5} \left( \frac{Ha^{1/2}}{\Phi} \right) \quad (4)$$

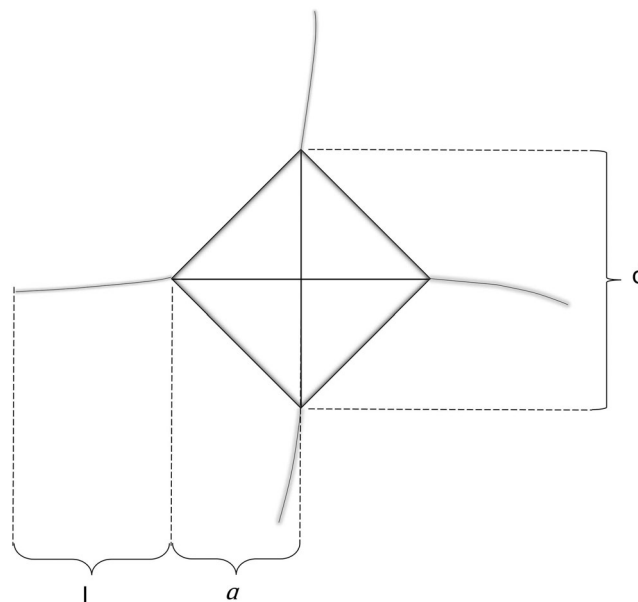


FIGURE 3 Vickers indentation schematic representation

where  $l$  is the average length of the cracks,  $a$  is the half average length of the diagonals of the indenter impression,  $E$  is the elastic modulus, and  $\Phi$  is a constant ( $\sim 3$ ).

Finally, approximately 10 bar samples for each composition were polished down to  $3 \times 4 \times 45$  mm<sup>3</sup> for fracture toughness tests according to the ISO 23146 standard.<sup>26</sup> The samples were ground flat on  $4 \times 45$ - and  $3 \times 45$ -mm<sup>2</sup> faces using a 150-mesh sandpaper, and the finishing was performed similarly as described in the previous section with B3B disc samples, but using additional sandpapers (600 and 1200 mesh) on the  $4 \times 45$ -mm<sup>2</sup> faces. All sample corners were polished off. The specimens were then glued side by side on a metallic plate using resin. They had their length carefully measured and a straight line drawn in their centers using a pencil. With a thin diamond saw, we inserted a “starter notch” along the pencil line until it was  $\sim 0.5$  mm in depth.

After this step, we used a 3- $\mu$ m diamond paste (Arotec) and a standard razor blade in the starter notch to increase its depth to 0.8–1.2 mm by performing back-and-forth movements. The samples were carefully cleaned with acetone in an ultrasonic bath (Elma, Elmasonic P) for  $\sim 2$  min.

The  $K_{Ic}$  tests were conducted in a universal testing machine (MTS, criterion model 43) with the samples carefully positioned on the loading spans (40 and 20 mm); notches facing down. The tests were carried out at a speed of 0.5 mm/min in a humidity range of 40%–44%.

After each test, the samples were immediately observed by OM (Nikon, Eclipse LV100N POL) to measure the notch size and find out whether a subcritical crack growth zone was present or not, that is, a region where a crack

propagates even when the critical stress factor is smaller than the intrinsic fracture toughness, and it is usually intensified by environmental factors such as humidity.<sup>2</sup> The fracture toughness was calculated through the following equation:

$$K_{Ic, SEVNB} = \frac{F_f}{B\sqrt{W}} \cdot \frac{S_1 - S_2}{W} \cdot \frac{3\sqrt{\alpha}}{2(1 - \alpha)^{1.5}} \cdot Y^*, \quad (5)$$

where  $Y^*$  is calculated through the following equation:

$$Y^* = 1.9887 - 1.326\alpha - \frac{(3.49 - 0.68\alpha + 1.35\alpha^2)\alpha(1 - \alpha)}{(1 + \alpha)^2}, \quad (6)$$

where  $K_{Ic, SEVNB}$  is the fracture toughness (MPa m<sup>1/2</sup>),  $F_f$  is the fracture load (MN),  $B$  is the test piece width (m),  $W$  is the test piece depth (m),  $S_1$  is the support span (m),  $S_2$  is the loading span (m),  $\alpha$  is the relative V-notch depth ( $c/W$ , where  $c$  is the average V-notch depth [m]), and  $Y^*$  is the stress intensity shape factor. Equations (5) and (6) are provided in Ref. [26].

### 3 | RESULTS AND DISCUSSION

#### 3.1 | Glasses

After casting and annealing at 50°C below  $T_g$ , the glasses on the left side of the immiscibility dome (Figure 1) were bluish with some white, translucent areas (Figure 4A); therefore, the phase separation process occurred during the casting operation. The spinodal samples had a similar aspect, but with larger white opaque areas.

As the exact limits of the PbO-rich portion of the LLPS region are not certain, we tested three glass compositions until we visually found clear signs of the phase separation process (Figure 4B). The cylinder on the left side is the binodal-2 composition, B2, the one in middle is the binodal-2' composition, B2', and the one on the right side is the glass OTG.

It is important to note that cylindrical molds were initially used to obtain the glasses; however, because of the very prominent shrinking (appearing as “cones” inside the cylinders, as it can be seen in Figure 4B) and the excessive cracking of glasses on the PbO-rich side, we decided to obtain glass samples directly from shallow disc molds (Figure 4C). A spinodal sample obtained using this mold is shown in Figure 4D.

Table 2 shows the glass transition temperatures,  $T_g$ , obtained by DSC. Figure 5 shows the DSC curves. Although the LLPS glasses have two phases, only one glass transition temperature could be observed. This probably occurs because the matrix phase predominates as a result of its

TABLE 2 Glass transition temperatures obtained by differential scanning calorimetry (DSC) at 10°C/min

Composition	$T_g$ (°C)
B1' (boron-rich matrix)	285
B1 (boron-rich matrix)	300
Spinodal	272
B2 (Pb-rich matrix)	425
OTG (Pb-rich glass)	440

Abbreviation: OTG, outside the gap.

significantly higher volume fraction, except for the spinodal glass, for which there is a similar content of both phases. However, also in this case, only one  $T_g$  was observed at a relatively low temperature (compared with the Pb-rich glass), indicating that the B-rich phase, which has the lowest  $T_g$ , was detected. Hence, the annealing heat treatments were conducted at 50°C below the  $T_g$  of the glassy matrix.

#### 3.2 | Microstructures (SEM-EDS)

Figure 6 shows the microstructures obtained using the backscattered electron mode and the EDS spectra of samples of the B1, spinodal, B2, and OTG compositions, respectively. The EDS spectra are related to two regions: A (bright part) and B (dark part). As the OTG glass is homogeneous, only the spectrum of region A is shown. It is important to note that all these samples underwent an initial heat treatment for 2 h at 50°C below  $T_g$  to minimize the macro stress level to allow sample handling. Note that we are referring to the normal macro stresses that all glasses undergo as a result of thermal gradients during cooling. The residual stress due to the thermal and elastic mismatches of the two phases cannot be relieved by thermal annealing. Most of the LLPS appeared during the cooling path of the SCL, and perhaps some during this annealing treatment.

The samples did not show any visual sign of degradation; however, considering the high boron content of the B1' and B1 compositions, it is reasonable to assume that they could have some surface defects due to atmospheric attack.

The sample B1 (Figure 6A) shows particles with an average diameter of ~60 nm. This estimate was made using the Fiji image processing software, which also shows that these particles represent ~23% of the glass volume. Comparing the compositions of the particles and the matrix, the bright contrast particle area has more Al than the dark contrast matrix area. There are no clear differences in B and Pb. It is important to note that the sensitivity to light elements, especially Boron, is poor in EDS analysis. The Pb concentration in the B1 composition may be too low to detect the

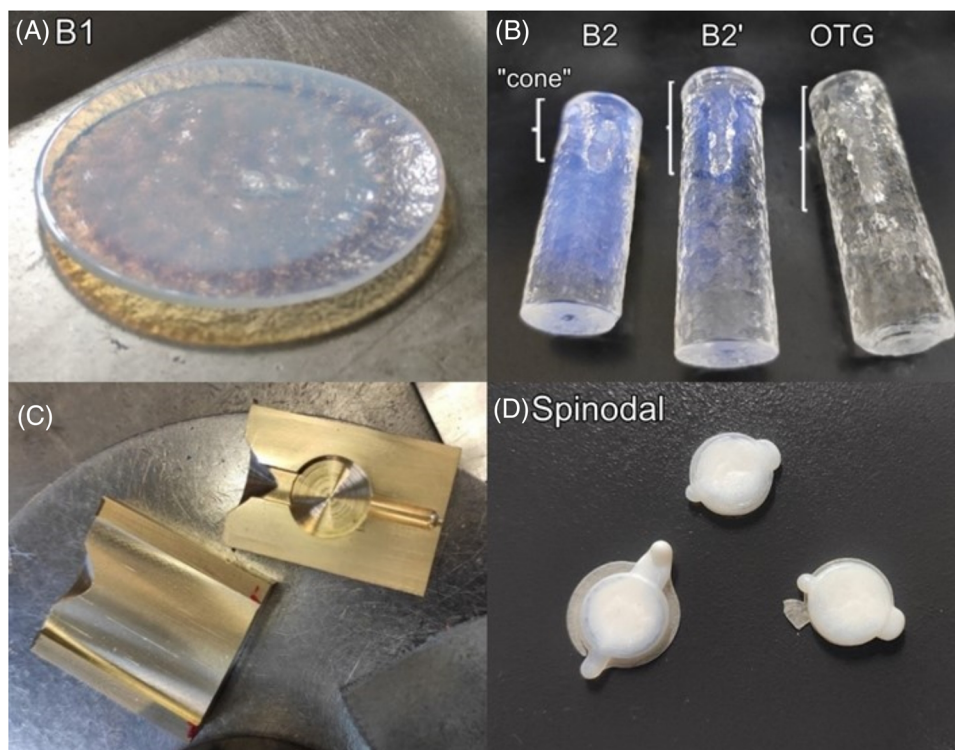


**FIGURE 4** (A) Binodal-1 glass obtained by splat cooling; (B) compositions on the PbO-rich side of the PbO–B<sub>2</sub>O<sub>3</sub>–Al<sub>2</sub>O<sub>3</sub> immiscibility curve—side by side for comparison (right); (C) mold (left) used to obtain disc samples; (D) spinodal samples (this picture was taken before any heat treatment)

difference between the particles and the matrix. However, from the contrast point of view, it is obvious that the bright contrast particle area has a higher average atomic number than the dark contrast matrix area. Therefore, the particles are PbO-rich embedded in a matrix consisting mainly of B<sub>2</sub>O<sub>3</sub>.

Figure 6B shows a typical spinodal micrograph consisting of intertwined structures. The Fiji image analysis shows a ratio of 48/52 between the two phases, as expected for typical spinodal microstructures. The bright contrast area has more Al and Pb than the dark contrast area. Although there are no clear differences in B, the areas richer in Pb and Al should be poorer in B. Thus, it can be concluded that the spinodal composition has a typical spinodal structure composed of a PbO-rich area and a B<sub>2</sub>O<sub>3</sub>-rich area.

Figure 6C shows the B2 composition, which is located on the other side of the miscibility gap (Figure 1). It shows particles with dark contrast, contrary to the B1 composition. Comparing the composition of the particles and the matrix, the bright contrast matrix area has more Al and Pb than the dark contrast particle area. Therefore, for glass B2, the matrix has more PbO and Al<sub>2</sub>O<sub>3</sub>, whereas the particles have more B<sub>2</sub>O<sub>3</sub> than the other compositions. Furthermore, the particles in the B2 composition are smaller than those in the B1 composition (40 nm average diameter),

which agrees with their visual aspect: The B1 glass has a whitish appearance, whereas the B2 glass has a subtle bluish one (Figure 4). The image analysis showed that the particles correspond to ~27% of the volume.

Finally, Figure 6D shows the micrograph of the OTG composition. No microstructure could be observed, indicating that the LLPS phenomenon does not occur in this composition.

Here we address the Pt-peak that it is visible in all graphs of Figure 6. Although all samples were coated with Pt for our measurements, we note that these glasses were obtained using Pt crucibles, and thus contamination cannot be completely discarded. However, the choice of our starting chemicals (H<sub>3</sub>BO<sub>3</sub> and Pb<sub>3</sub>O<sub>4</sub>) was such to avoid contaminations, because an oxidative atmosphere was created, and the situation where Pb<sub>3</sub>O<sub>4</sub> is reduced to Pb that could attack the Pt-crucible was small. However, even in case of contamination with Pt, the amount would not be large enough to affect the mechanical properties.

### 3.3 | Flexural strength (B3B tests)

The flexural strength values using B3B tests for each composition and conditions used are shown in Table 3 and

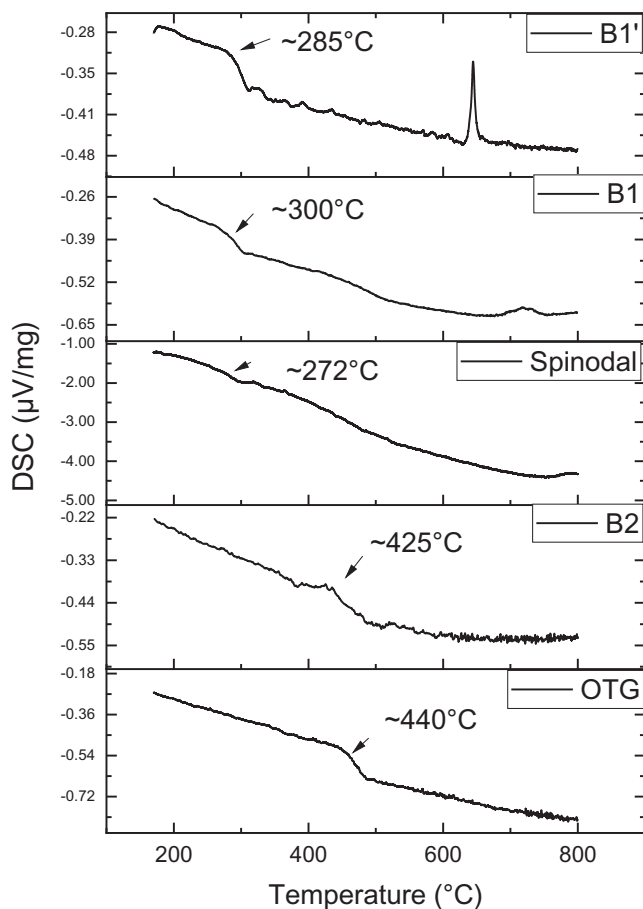


FIGURE 5 Differential scanning calorimetry (DSC) curves for all glasses in this study obtained by using a heating rate of  $10^{\circ}\text{C}/\text{min}$

Figure 7. The elastic modulus and Poisson's ratio values used in our calculations are shown in Table 4. They were estimated using the SciGlass software.

Flexural strength, as measured by the B3B tests, increases toward the center of the immiscibility dome, with the Spinodal composition showing the highest strength by far. The additional treatment at  $T_g$  for 1 h (to further develop the phase separation that started in the cooling path) presented only a minor effect, except for the B2 composition, where the  $S_f$  value decreased.

A pertinent observation concerns the number of pieces into which the glass discs shattered after the B3B tests. Börger et al.<sup>31</sup> reasonably linked the number of fractured pieces as a measure of the stored elastic energy immediately before the fracture event. In other words, the number of fractured pieces should increase with material strength.<sup>31</sup> The B2 and OTG discs always fractured into only two pieces (Figure 8, left), approximately in the disk center, whereas the other discs fractured into, at least, four pieces. We also noticed many microcracks in all pieces of the B2 composition cross-sectional samples under an OM after the B3B tests (Figure 8, right).

TABLE 3 Compositions, conditions used, flexural strength results by B3B tests, and standard error

Compositions	Conditions	Flexural strength (B3B) (MPa)
B1'	No heat treatment	$97 \pm 4$
	Treated at $T_g/1$ h	$99 \pm 6$
B1	No heat treatment	$104 \pm 7$
	Treated at $T_g/1$ h	$112 \pm 6$
Spinodal	No heat treatment	$157 \pm 5$
	Treated at $T_g/1$ h	$166 \pm 7$
B2	No heat treatment	$95 \pm 3$
	Treated at $T_g/1$ h	$82 \pm 2$
OTG	No heat treatment	$80 \pm 3$
	Treated at $T_g/1$ h	$85 \pm 3$

Abbreviation: OTG, outside the gap.

TABLE 4 Elastic moduli (GPa) and Poisson's ratios of all glasses (assuming they are free of liquid-liquid phase separation [LLPS]) estimated from the chemical composition using SciGlass

Composition	$E$ (GPa)	$\nu$
B1'	39	0.28
B1	42	0.28
Spinodal	47	0.28
B2	54	0.28
OTG	58	0.28

Abbreviation: OTG, outside the gap.

Although they may seem like crystals, it is important to note that no crystalline peak was found in the X-ray diffraction (XRD) measurements of the B2 glasses. Additionally, although the B2 and OTG compositions exhibited similar  $S_f$  results, the OTG samples did not show microcracking after the B3B tests. We believe that the type of residual stress in the matrix and the liquid droplets are some of the reasons why the B2 glass likely microcracked (Figure 9). The phase distributions for compositions at both ends of the gap are naturally quite different: In the *B1'* and *B1* compositions, the B-rich phase forms the matrix, and the droplets are the Pb-rich phase. The B-rich phase exhibits a higher thermal expansion coefficient ( $\sim 1 \times 10^{-5} \text{ K}^{-1}$ , estimated by the SciGlass software) than that of the Pb-rich phase ( $\sim 6 \times 10^{-6} \text{ K}^{-1}$ , estimated by SciGlass software); therefore, in this case, the inclusions should be under an isotropic *compressive stress* state, whereas the matrix should be subjected to radial compressive stress,  $\sigma_R$ , and tensile tangential stress,  $\sigma_T$  (Figure 9A), bearing in mind that the magnitudes of the tangential stresses are half those of the radial stresses. The opposite should occur in the specimens of the *B2 composition*: The matrix, or the Pb-rich phase, should be subjected to tensile radial stresses and



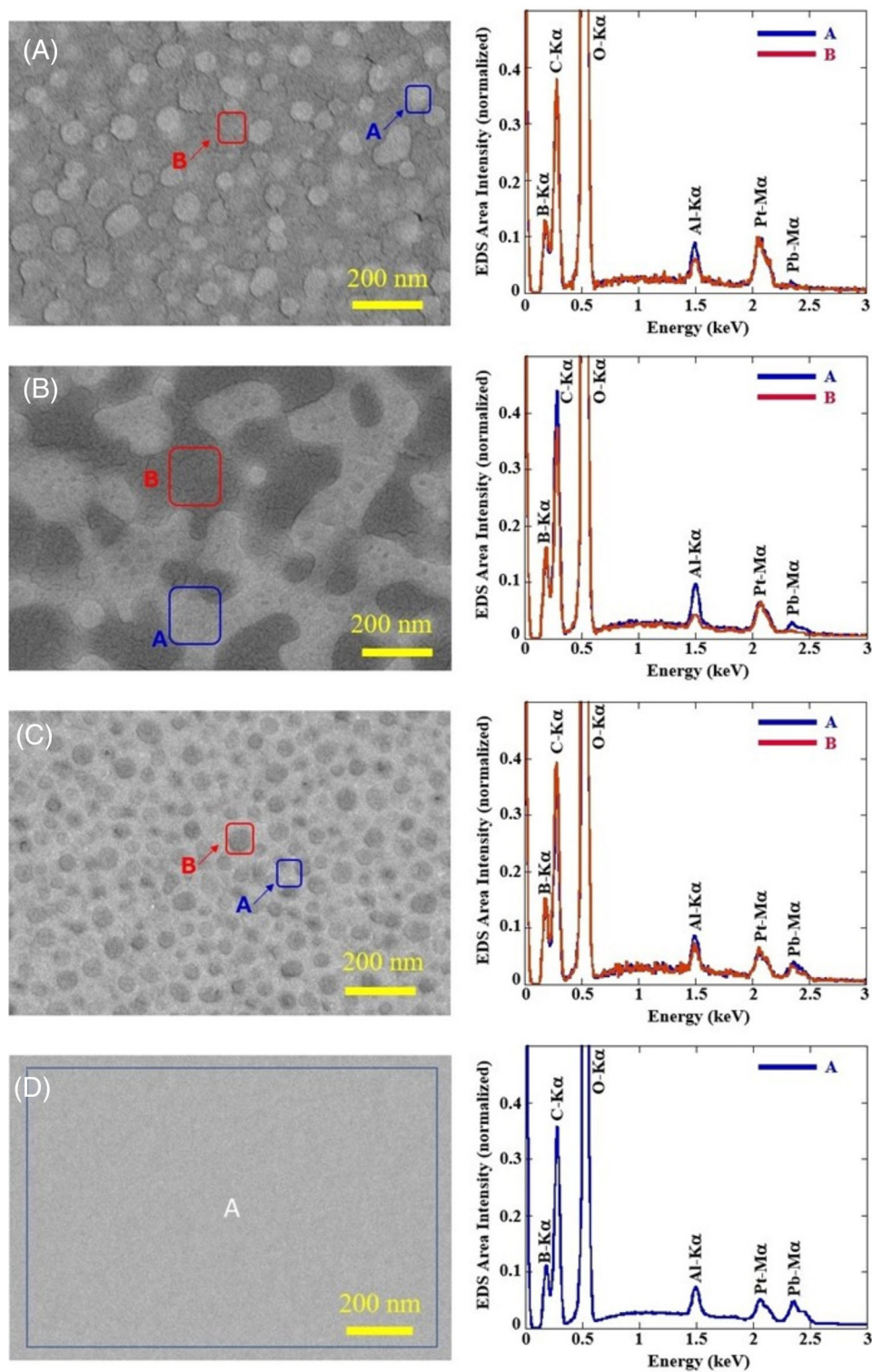


**FIGURE 6** (A) Binodal-1 (B1), (B) spinodal, (C) binodal-2 (B2), and (D) outside the gap (OTG) micrographs obtained in the backscattered electron (BSE) mode and the respective elements found through energy-dispersive X-ray spectroscopy (EDS)

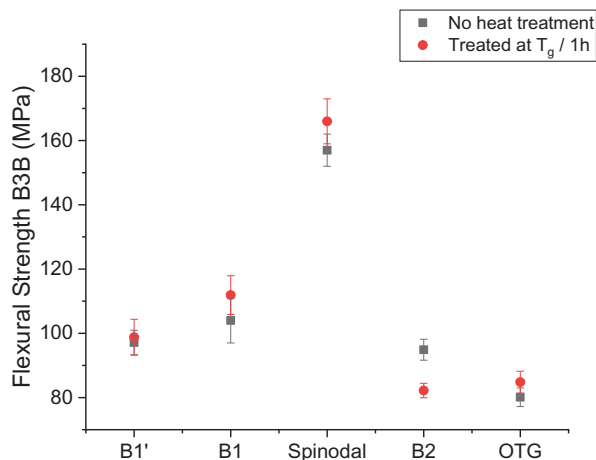


FIGURE 7 Flexural strength obtained by B3B tests for all the glasses and conditions used. The outside the gap (OTG) glass is outside the miscibility gap.

TABLE 5 Estimated residual stresses for the glasses showing liquid–liquid phase separation

Glass	Estimated residual stress in the inclusions (MPa)
B1'	–25 (compressive)
B1	–22 (compressive)
Spinodal	–/+ 14 <sup>a</sup>
B2	+77 (tensile)
OTG	0 = outside the miscibility gap

Abbreviation: OTG, outside the gap.

<sup>a</sup>The sign –/+ indicates that it depends on which phase is considered as matrix/inclusion.

compressive tangential stresses, whereas the inclusions (B-rich phase) should be under an isotropic *tensile stress* state (Figure 9B). Estimates using Equation (7), derived by Hsueh and Becher,<sup>34</sup> which is based on Selsing's model for internal stresses,<sup>35</sup> confirm this residual stress distribution (Table 5).

$$\sigma_{r-est} = \frac{\Delta_{CTE} \cdot \Delta T}{\left( \frac{1}{3K_i} + \frac{1}{4(1-f_i)G_m} + \frac{f_i}{3(1-f_i)K_m} \right)}, \quad (7)$$

where  $\Delta_{CTE} = CTE(\text{inclusion}) - CTE(\text{matrix})$  (CTE = coefficient of thermal expansion),  $\sigma_{r-est}$  is the estimated radial stress in the inclusion,  $\Delta T$  is the difference between the upper temperature stresses (the lowest  $T_g$  between the matrix and the inclusion) and the final temperature (usually room temperature),  $K_i$  is the bulk modulus of the inclusion,  $G_m$  is the shear modulus of the matrix,  $K_m$  is the bulk modulus of the matrix, and  $f_i$  is the volume fraction of the inclusions.  $K$  and  $G$  are obtained from SciGlass.

Table 5 shows the estimated residual stresses in the glassy particles for all compositions studied according to Equation (7). These residual stresses in the inclusions,  $\sigma_{rest}$ , have relatively small magnitudes.

In a previous work conducted with glass–ceramics (GCs) of the CaO–Li<sub>2</sub>O–SiO<sub>2</sub> system,<sup>37</sup> we noticed that, depending on the crystallized fraction of lithium metasilicate crystals embedded in a matrix consisting of wollastonite and residual glass, spontaneous microcracks were visible inside the lithium metasilicate crystals and, as a result, the strength and  $K_{Ic}$  decreased. Those results are an example of a system in which the inclusions (lithium metasilicate crystals) have a higher thermal expansion coefficient ( $\alpha_p = 15 \times 10^{-6} \text{ K}^{-1}$ ) than the matrix (wollastonite,  $\alpha_w = 6 \times 10^{-6} \text{ K}^{-1}$ , and the residual glass,  $\alpha_{rg} = 11 \times 10^{-6} \text{ K}^{-1}$ ). In this case, the cracks can propagate around or through the inclusions, depending on whether the matrix surface energy is lower or higher than that of the inclusions.<sup>36</sup>

The B2 samples showed spontaneous microcracking and evidence of low values of stored elastic energy (small number of fractured pieces after the B3B tests). These results suggest that there was excess stored energy, such that the glass spontaneously cracked to alleviate it. It is possible that this particular microstructural configuration, where the inclusions present a higher thermal expansion coefficient than that of the matrix and are under tensile stress, is prone to generate spontaneous cracking to release the residual stress, which can happen when the particles exceed a certain critical size.

Regarding this topic of residual stresses and strength of LLPS glasses, an anonymous reviewer of this manuscript observed that: “Häßler and Rüssel<sup>8</sup> claimed that residual stresses are responsible for the increase in bending strength; however, there is no clear relationship between the  $\Delta_{CTE}$  and bending strength in their data. In fact, plotting of their bending strength versus  $\Delta_{CTE}$  seems to present a weak negative correlation”. On this matter, we have demonstrated in recent articles addressing GCs<sup>38,39</sup> that the internal residual stresses, which result from the CTE mismatch between the crystals and the residual glass, do *not* explain the improved strength and toughness of the GCs. Residual stresses only explain decreased strength when they induce spontaneous cracking in GCs of relatively large grain size.<sup>38,39</sup>

Additionally, the cracks in the B2 composition, which appeared spontaneously, could have nucleated and propagated as a result of residual stress and the hygroscopicity of these borate glasses.<sup>40</sup> In any composition in the PbO–B<sub>2</sub>O<sub>3</sub>–Al<sub>2</sub>O<sub>3</sub> system, the B<sub>2</sub>O<sub>3</sub>-rich phase (inclusions or matrix) is less resistant to moisture attack. Miyata et al.<sup>11</sup> stated that glasses consisting of B<sub>2</sub>O<sub>3</sub>-rich inclusions in a PbO-rich matrix, as the B2 glass of this study, show



FIGURE 8 B3B fractured piece from the B2 sample treated at  $T_g$  for 1 h. Top (left) and cross-sectional (right) views of the sample showing a large number of microcracks

particles with lower resistance to moisture attack than the matrix. Considering the thermal expansion mismatch between the particles and the matrix ( $\alpha_i > \alpha_m$ ), the particles are submitted to tensile stress and, in this case, the growing crack can penetrate them, although according to those authors the crack tip can become locally blunted in the inclusion–matrix interface.

This scenario is similar to that of the B2 composition situated at the right-hand portion of the  $\text{PbO}-\text{B}_2\text{O}_3-\text{Al}_2\text{O}_3$  miscibility gap ( $\text{B}_2\text{O}_3$ -rich particles and  $\text{PbO}$ -rich matrix, Figure 9B). Therefore, one might initially think that this stress state could explain the lower flexural strength value of the  $\text{PbO}$ -rich B2 glass compared with the other compositions. However, as the OTG glass has no residual stresses caused by the thermal and elastic mismatches, the lower strength of these glasses most likely results from their high  $\text{PbO}$  content. For instance, Soga et al.<sup>41</sup> concluded that the increase in  $\text{PbO}$  in lead–borate glasses can decrease

another mechanical property, the  $K_{Ic}$ . We will discuss this matter in more detail later on in this article.

With heat treatment at  $T_g$ , an increase in droplet size and volume fraction would be expected in these phase-separated glasses. However, the flexural strengths of the B1 and B1' glasses, with or without further heat treatment, are the same within the error margin (Figure 7). Yet, the B2 glass shows a different trend: The sample submitted to heat treatment at  $T_g$  for 1 h exhibits a value lower than that of the sample not heat treated. One explanation for the different behaviors of the B2 glass is that the (supposed) increase in inclusion size potentialized spontaneous microcracking in a composition that, as a result of the thermal expansion mismatch between the inclusions and the matrix, already presented a tendency for such, as explained earlier. These microcracks and/or the residual tensile stress at the interface between droplets and matrix might contribute to the decreased flexural strength. It is also important to note that heat treatments potentially change not only the particle size, but also their number, the matrix composition, and the phase concentration.

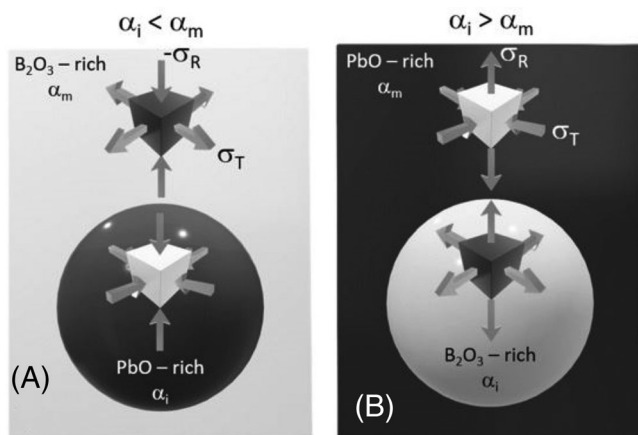


FIGURE 9 Scheme of the residual stress state expected for the (A) binodal-1 and (B) binodal-2 glasses Source: After Ref. [36]

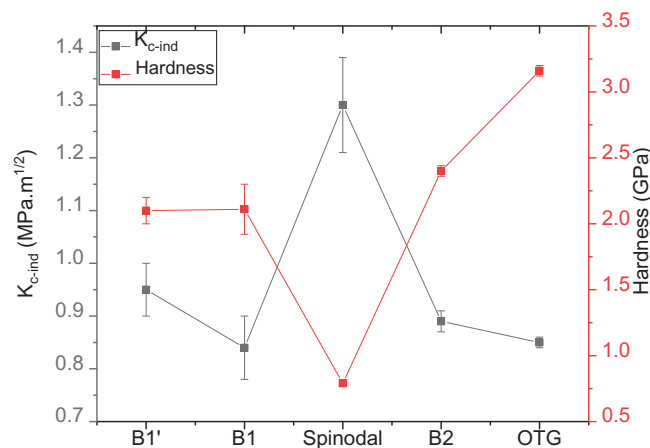
### 3.4 | The Vickers hardness and indentation toughness

Table 6 and Figure 10 show the hardness and indentation toughness ( $K_{c-ind}$  obtained by the Vickers tests) results for all compositions. It is important to note that all glass samples were measured under the same conditions for a reliable comparison: 30 N for 15 s loading time. Such a high load had to be used because the B2 glass does not show any crack in the impression corners indented with lower loads. We observed the presence of lateral cracks and spalling in some compositions. In addition, the crack type (Palmqvist, HalfPenny, etc.) may have varied, not only due

**TABLE 6** Vickers test results for all compositions studied in this work

Composition	Hardness (GPa)	$K_{c-ind}$ (MPa m <sup>1/2</sup> )
B1'	2.1 ± 0.1	0.95 ± 0.05
B1	2.1 ± 0.1	0.84 ± 0.06
Spinodal	0.8 ± 0.1	1.37 ± 0.06
B2	2.4 ± 0.1	0.89 ± 0.02
OTG	3.2 ± 0.1	0.85 ± 0.01

Abbreviation: OTG, outside the gap.

**FIGURE 10** Average hardness (red squares) and  $K_{c-ind}$  (black squares) obtained by the Vickers tests for all compositions studied using a load of 30 N for 15 s

to the relative crack length ( $l/a$ ), but also for different glass compositions. Thus, some of these occurrences can affect the mechanical properties, such that we should consider the results presented in Table 6 with caution.

The spinodal composition exhibited by far the largest  $K_{c-ind}$ , which seems to be accompanied by a significant decrease in hardness. The cracks generated by indentation on the spinodal sample surface are smaller and thinner than those observed in the other compositions and often do not follow a straight line.

Quite different indentation patterns were found for each composition (Figure 11). However, the most distinguished indentation impressions were obtained for the spinodal glasses (Figure 11C), which precluded the measurement of the impression diagonals and crack lengths. We solved this problem by eliminating a certain surface layer of the specimens, as explained later. Fabris et al.<sup>42</sup> reported similar impression morphology, obtained by the Vickers indentation, in a GC with a surface crystallized layer under high compressive residual stress. We conducted XRD tests and did not observe any crystal phase in the spinodal samples. Thus we decided to use the same sample in further tests after removing its external layer (~1 mm) to verify whether the bulk and surface of this sample presented a microstruc-

**TABLE 7**  $K_{Ic-SEVNB}$  results for four different compositions

Composition	$K_{Ic}$ (MPa m <sup>1/2</sup> )-SEVNB
B1 (binodal)	1.04 ± 0.09
Spinodal	1.60 ± 0.10
B2 (binodal)	0.86 ± 0.05
OTG (no LLPS)	0.82 ± 0.08

Abbreviations: LLPS, liquid-liquid phase separation; OTG, outside the gap; SEVNB, single-edge V-notch beam.

tural gradient, as gradients have been observed in LLPS sodium borosilicate glasses.<sup>6</sup>

For lower loads, such as 1, 5, and 10 N, we observed a more common impression shape after indentation. However, for loads  $\geq 15$  N, the samples started to present spalling, where certain amounts of material are removed from the surface around the indentation impression. Spalling is very common in tempered glasses because of their deep compressive field, and it is more frequent when high loads are used. The compressive stress changes the crack path, causing it to propagate toward the surface instead of downward and in the material.<sup>43</sup>

We also used another sample from the same batch to investigate if its impression behavior was the same. The new sample was submitted to the same polishing process used previously. Spalling was once again observed when loads  $> 15$  N were used. When we removed the external layer of this second sample (~1 mm), indentations with better reproducibility were generated (Figure 11D), and we managed to measure the cracks to finally estimate  $K_{c-ind}$  for the spinodal glass (Table 6).

### 3.5 | $K_{Ic}$ tests (SEVNB)

$K_{Ic}$  tests were conducted in three compositions exhibiting LLPS (B1 is richer in  $B_2O_3$ , spinodal; and B2 is richer in PbO) and in one composition outside the immiscibility dome, OTG.

In the B2 and OTG glasses, an area that can be interpreted as a subcritical crack growth zone could be found in almost all samples. According to the ISO 23146 standard, this subcritical crack growth zone should be added to the V-notched surface size to compose the  $c$  value. The ISO standard also suggests the use of a dry nitrogen atmosphere if subcritical growth zone is observed, but we could not assemble the needed equipment; thus, only the results obtained in air at room temperature are reported. The  $c$  size was measured in three different points equally distant from each other, and an average value was considered. For a four-point test,  $K_{Ic-SEVNB}$  was calculated through Equations (5) and (6). The results are shown in Table 7.

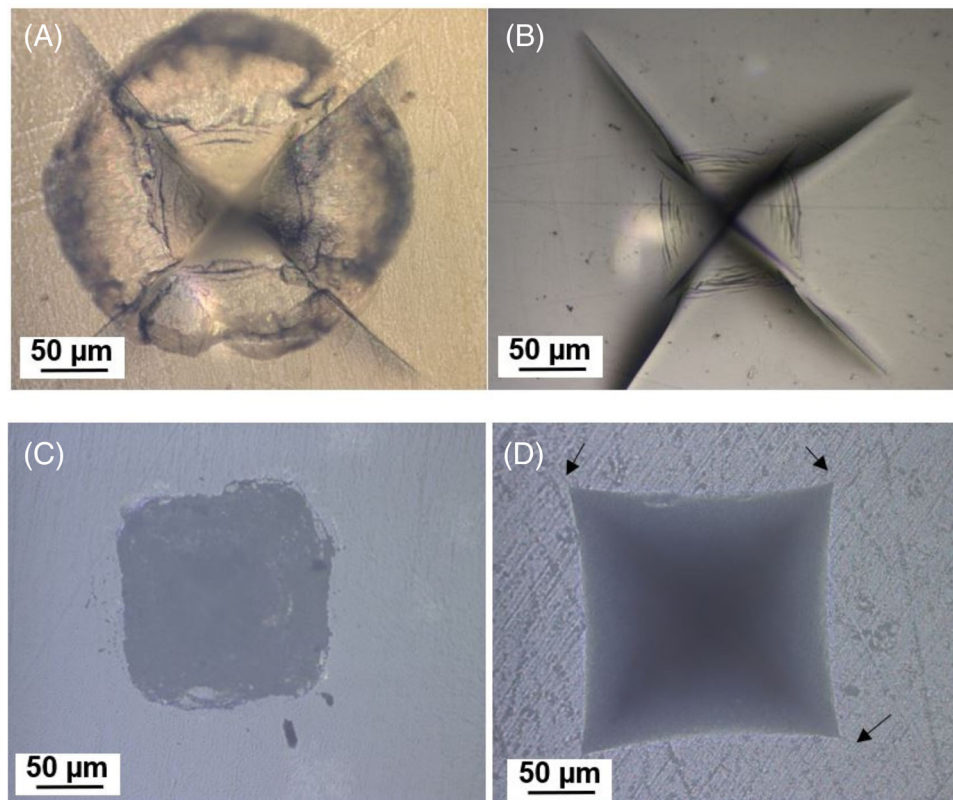


FIGURE 11 Vickers indenter impressions with a 30-N load for 15 s in the (A) B1 and (B) B2 glasses, (C) spinodal glass, and (D) spinodal glass after removal of an external layer of  $\sim 1$  mm. The black arrows show cracks.

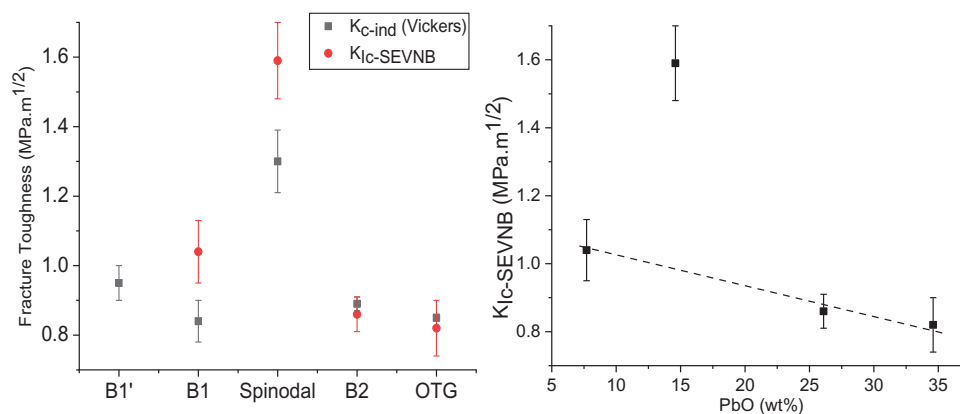


FIGURE 12 (A) Comparison between the  $K_{c-ind}$  values (black squares), obtained by the Vickers tests, and the more rigorous  $K_{IC-SEVNB}$  values (red circles); (B) dependence of  $K_{IC-SEVNB}$  on PbO content. Except for the spinodal composition ( $\sim 14$ -wt% PbO), there is a slight decrease in  $K_{IC}$  with increasing PbO. The dashed line is only a guide to the eyes.

These values exhibit a similar trend to that of the  $K_{c-ind}$  values (Figure 10), with the spinodal composition value being  $\sim 50\%$  higher than that of the B1 glass, and 90% higher than those of the B2 and OTG glasses (Figure 12).

As the  $K_{IC-SEVNB}$  values for the B2 (binodal) and OTG (no phase separation) glasses are similar despite the large microstructural differences, it seems that the presence of

binodal LLPS is not relevant for the mechanical properties in this case. Additionally, except for the spinodal composition (Figure 12B), it is also possible to observe a decrease in  $K_{IC-SEVNB}$  with increasing PbO. Soga<sup>41</sup> discussed the effect of PbO added to  $B_2O_3$  glasses. The introduction of Pb changes the boron ion coordination from 3 to 4, which decreases  $K_{IC}$ . Konijnendijk and Verweij<sup>44</sup> studied

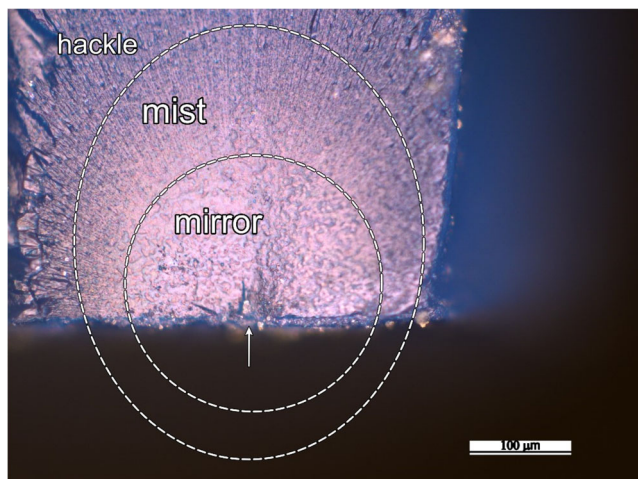


FIGURE 13 Fractured B1 glass piece after B3B test showing the mirror, mist, and hackle limits

PbO–B<sub>2</sub>O<sub>3</sub> glasses by Raman spectroscopy, and found “boroxol” groups ( $\sim 805\text{ cm}^{-1}$ , B–O rings in three coordination) in vitreous PbO–3B<sub>2</sub>O<sub>3</sub>, but not in PbO·2B<sub>2</sub>O<sub>3</sub> glass, which could explain the difference in  $K_{Ic}$  as the PbO content increases. Shinkai and Ishikawa<sup>45</sup> measured the  $K_{Ic}$  of glasses outside the miscibility gap (PbO-rich) and confirmed that  $K_{Ic}$  decreased with increasing the PbO content, probably reflecting this type of structural change. Thus, Figure 12 provides additional evidence that the increase in  $K_{Ic-SEVNB}$  for the spinodal composition is due to its microstructural effect rather than to a compositional effect.

Finally, our results of  $S_f$  and  $K_{Ic}$  are similar to those reported by Miyata and Jinno for PbO–B<sub>2</sub>O<sub>3</sub> glasses<sup>12</sup> (no Al<sub>2</sub>O<sub>3</sub>). Hence, the addition of Al<sub>2</sub>O<sub>3</sub> narrows the miscibility gap down but does not seem to have a significant effect on the mechanical properties of these lead–borate glasses (and they all have the same alumina content, 7 wt%). The elastic moduli estimated by SciGlass software for our glasses are somewhat higher than those found by Shaw and Uhlmann,<sup>25</sup> but as we did not directly measure this property, we cannot make further speculations about this discrepancy.

### 3.6 | Fracture analysis and stress estimates

Fracture surface analysis can be used to identify the causes of material failure by locating the origin of fracture and determining characteristic fracture patterns, such as mirror radius, mist, and hackle.<sup>32</sup> Figure 13 shows one of our samples (B1 glass), which exemplifies the limits of the different characteristic regions within a fractured glass piece.

TABLE 8 Values of the  $A$  constant estimated from Shinkai and Ishikawa’s data<sup>45</sup> for the compositions used in this work

Composition	$A$ (MPa m <sup>1/2</sup> )
B1′	2.36
B1	2.30
Spinodal	2.22
B2	2.07
OTG	1.94

Abbreviation: OTG, outside the gap.

TABLE 9 Estimated stress at the point of fracture for the B1′, B1, and spinodal glasses with no heat treatment and treated at  $T_g$  for 1 h

Composition	Composition/ condition	Estimated $\sigma_r$ (MPa)
B1′	As cast	$75 \pm 14$
	Treated at $T_g/1\text{ h}$	$66 \pm 9$
B1	As cast	$58 \pm 12$
	Treated at $T_g/1\text{ h}$	$47 \pm 8$
Spinodal	As cast	$30 \pm 5$
	Treated at $T_g/1\text{ h}$	$9 \pm 9$

Classical works by Mecholsky et al.<sup>46,47</sup> have validated the use of Equation (2). Shinkai and Ishikawa<sup>45</sup> measured the  $A$  constant for PbO–B<sub>2</sub>O<sub>3</sub> glasses outside the miscibility gap and found  $A = 1.70$  for a glass of composition 30-mol% (58-wt%) PbO–70-mol% (42-wt%) B<sub>2</sub>O<sub>3</sub> and  $A = 0.65$  for one of compositions 70-mol% (88-wt%) PbO–30-mol% (12-wt%) B<sub>2</sub>O<sub>3</sub>. We were able to extrapolate from these data for our compositions (Table 8) and, although our glasses are somewhat different (they have 7-wt% Al<sub>2</sub>O<sub>3</sub>), calculations with our experimental data showed that the use of their data to achieve the  $A$  constant is a reasonable approximation.

As previously explained, we performed B3B tests on an average number of 8–12 samples for each composition/heat-treatment condition, and the same samples were used for this fracture analysis. Their average flexural strength value was considered  $\sigma_a$ . Of all these samples, usually three or more could not be analyzed because of at least one of the following factors: surface degradation due to humidity attack and difficulty in finding the fracture origin in samples that shattered into too many pieces.

Table 9 shows the estimates for the stress at the fracture point according to Equation (2) for three compositions—B1′, B1, and spinodal—using two different conditions: as cast and heat treated at  $T_g$  for 1 h. It is important to note that the stress values in Table 9 are not the same as the residual stresses calculated by Equation (7) (Table 5).

The spinodal glass shows the lowest stress at the fracture point. The mirror radius of the B2 and OTG glasses could not be measured because of the difficulties in

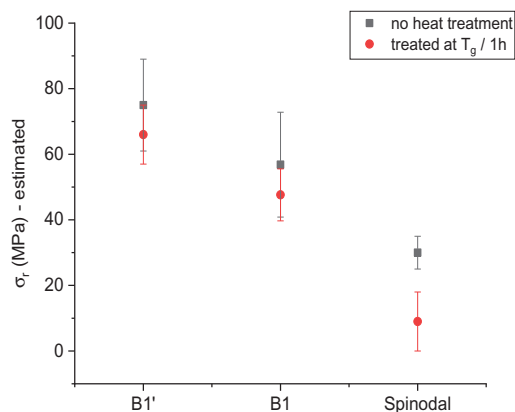


**FIGURE 14** Estimates of stress at the point of fracture; average values for the B1', B1, and spinodal compositions

identifying the characteristic fracture patterns: mirror, mist, and hackle.

Figure 14 shows the average values of the stress at the point of fracture.

Although these are only estimates, it is possible to observe a clear trend that the stress at the fracture point decreases as the composition approaches the spinodal dome.

As previously mentioned, the B3B tested B2 and OTG samples always fractured in only two pieces, and their fracture regions were usually clear of defects and other typical patterns. The greater the stress in the origin of the fracture, the higher the stored energy just before fracture, and the richer the fracture markings.<sup>32</sup> It is possible that some type of microcracking occurred in these samples prior to our tests (one example is shown in Figure 8), releasing the residual stress and decreasing the stored energy. This also could explain the relatively low flexural strength and fracture toughness of these samples. Overall, it is likely that the intricate microstructure exhibited by the spinodal glass is dominant to its improved mechanical properties. Their typical snakelike structure, with ~50/50% of each phase, is much highly interconnected, much more than the droplet microstructure of most LLPS compositions.

#### 4 | CONCLUSIONS AND PERSPECTIVES

We studied four compositions of the PbO–B<sub>2</sub>O<sub>3</sub>–Al<sub>2</sub>O<sub>3</sub> system inside the miscibility gap (B1', B1, spinodal, and B2). These compositions were designed in such a way that the amorphous particles are under compressive residual stresses in some and under tensile residual stresses in others. We also made one glass OTG. Considering only the binodal compositions, which have droplet

microstructures, the B<sub>2</sub>O<sub>3</sub>-rich B1' and B1 glasses exhibited  $S_f$  and  $K_{IC}$  somewhat superior to those of the PbO-rich B2 glass and the OTG.




The spinodal glass showed the lowest level of residual stress and, by far, the best mechanical properties. Its  $K_{IC-SEVNB}$  and  $S_f$  values are almost twice those of the other glasses. This is the clearest result of this research work, which bears no speculations. These improved mechanical properties are likely caused by the high volume fractions and extensive interconnectivity of the two phases. Overall, the relatively low level of internal residual stresses in these lead–borate glasses had a negligible effect on toughening; microstructural effects being most relevant. This research work validates the concept that LLPS provides a feasible strategy to improve the mechanical properties of glasses.

One could also evaluate the effects of atomistic structure, size, and morphology of the second phase, and other features on the mechanical properties. To this end, computer modeling could help unveil the microscopic mechanisms of toughening in LLPS glasses. We hope the experimental results of this article will promote further research to understand and improve the strength and toughness of glassy materials.

#### ACKNOWLEDGMENTS

The authors thank Professor Francisco C. Serbena for the helpful discussions about the  $K_{IC}$  tests. We are also grateful to FAPESP (São Paulo Research Foundation Process no. 2013/07793-6) and to CNPq (National Council for Scientific and Technological Development 304734/2020-9) for partially supporting this research work.

#### ORCID

Gisele G. Santos  <https://orcid.org/0000-0001-7136-5494>  
 Satoshi Yoshida  <https://orcid.org/0000-0002-5231-4605>  
 Edgar D. Zanotto  <https://orcid.org/0000-0003-4931-4505>

#### REFERENCES

1. Varshneya AK. Fundamentals of inorganic glasses. Boston: Academic Press; 1994.
2. Feng W, Bonamy D, Célerié F, Fossati PCM, Gossé S, Houizot P, et al. Stress corrosion cracking in amorphous phase separated oxide glasses: a holistic review of their structures, physical, mechanical and fracture properties. *Corros Mater Degrad*. 2021;2:412–46.
3. Zanotto ED. Effect of liquid phase separation on crystal nucleation in glass-formers. Case closed. *Ceram Int*. 2020;46:24779–91.
4. Golovchak R, Thapar P, Ingram A, Savytskii D, Jain H. Influence of phase separation on the devitrification of 45S5 bioglass. *Acta Biomater*. 2014;10:4878–86.
5. Doremus RH, Turkalo AM. Phase separation in pyrex glass. *Science*. 1969;164:418–9.

6. Utsumi Y, Sakka S, Tashiro M. Experimental study on the bending strength of glass in relation to liquid-liquid phase separation. *Glass Technol.* 1970;11(3):80–5.
7. Seal AK, Chakraborti P, Roy NR, Mukherjee S, Mitra MK, Das GC. Effect of phase separation on the fracture toughness of  $\text{SiO}_2\text{-B}_2\text{O}_3\text{-Na}_2\text{O}$  glass. *Bull Mater Sci.* 2005;28:457–60.
8. Häßler J, Rüssel C. Effect of microstructure of a phase separated sodium-borosilicate glass on mechanical properties. *Ceram Int.* 2017;43:11403–9.
9. Cheng S, Song C, Ercius P, Cionea C, Hosemann P. Indentation cracking behaviour and structures of nanophase separation of glasses. *Phys Chem Glasses: B.* 2017;58:237–42.
10. Simmons CJ, Freiman SW. Effects of phase separation on crack growth in borosilicate glass. *J Non-Cryst Solids.* 1980;38–39:503–8.
11. Miyata N, Takeda S i, Jinno H. Slow crack growth in phase-separated glasses. *J Non-Cryst Solids.* 1987;95–96:1047–54.
12. Miyata N, Jinno H. Strength and fracture surface energy of phase-separated glasses. *J Mater Sci.* 1981;16:2205–17.
13. Miyata N, Jinno H. Use of Vickers indentation method for evaluation of fracture toughness of phase-separated glasses. *J Non-Cryst Solids.* 1980;38–39:391–6.
14. Sproull JF, Rindone GE. Correlation between strength of glass and glassy microphases. *J Am Ceram Soc.* 1973;56:102–3.
15. Zhang Q, Jensen LR, Youngman RE, To T, Du T, Bauchy M, et al. Influence of phase separation microstructure on the mechanical properties of transparent modifier-free glasses. *J Non-Cryst Solids.* 2022;595:121806.
16. Tang L, Krishnan NMA, Berjikian J, Rivera J, Smedskjaer MM, Mauro JC, et al. Effect of nanoscale phase separation on the fracture behavior of glasses: toward tough, yet transparent glasses. *Phys Rev Mater.* 2018;2:113602.
17. Christensen JFS, Sørensen SS, To T, Bauchy M, Smedskjaer MM. Toughening of soda-lime-silica glass by nanoscale phase separation: molecular dynamics study. *Phys Rev Mater.* 2021;5:093602.
18. Mecholsky JJ. Toughening in glass ceramics through microstructural design. In: Bradt RC, Evans AG, Hasselman DPH, Lange FF, editors. *Fracture Mechanics of Ceramics 6.* New York: Plenum Press; 1983 p. 165–180.
19. Martel L, Allix M, Millot F, Sarou-Kanian V, Véron E, Ory S, et al. Controlling the size of nanodomains in calcium aluminosilicate glasses. *J Phys Chem C.* 2011;115:18935–45.
20. Liedberg DJ, Ruderer CG, Bergeron CG. Evidence of metastable immiscibility in the system  $\text{PbO-B}_2\text{O}_3$ . *J Am Ceram Soc.* 1965;48:440.
21. Simmons JH. Miscibility gap in the system  $\text{PbO-B}_2\text{O}_3$ . *J Am Ceram Soc.* 1973;56:284–5.
22. Geller RF, Bunting EN. The system  $\text{PbO-B}_2\text{O}_3$ . *J Res Nat Bur Stand.* 1937;18:585–93.
23. Inoue S, Wada K, Nukui A, Yamane M, Shibata S, Yasumori A, et al. Estimation of phase separation rates of  $\text{PbO-B}_2\text{O}_3$  melts. *J Mater Res.* 1995;10:1561–4.
24. Shaw RR, Uhlmann DR. Effect of phase separation on the properties of simple glasses I. Density and molar volume. *J Non-Cryst Solids.* 1969;1:474–98.
25. Shaw RR, Uhlmann DR. Effect of phase separation on the properties of simple glasses II. Elastic properties. *J. Non-Cryst. Solids.* 1971;5:237–63.
26. International Standard ISO 23146. Fine ceramics (advanced ceramics, advanced technical ceramics)—test methods for fracture toughness of monolithic ceramics—single-edge V-notch beam (SEVNB) method. 2008
27. Podlesny J, Weinberg MC, Neilson GF, Chen A. Experimental determination of the binodal temperature in the lead borate system. *J Mater Sci.* 1993;28:1663–6.
28. Craievich AF. Small angle X-ray scattering study of phase separation of  $\text{B}_2\text{O}_3\text{-PbO-Al}_2\text{O}_3$  glass. *Phys Chem Glasses.* 1975;16(6):133–8.
29. Olivieri JR. Decomposição espinodal durante o resfriamento contínuo no sistema  $\text{B}_2\text{O}_3\text{-PbO-Al}_2\text{O}_3$  [Spinodal decomposition during continuous cooling in the  $\text{B}_2\text{O}_3\text{-PbO-Al}_2\text{O}_3$  system]. Master's thesis. São Carlos (Brazil): University of São Paulo; 1979;
30. Zarzycki J, Naudin F. Spinodal decomposition in the  $\text{B}_2\text{O}_3\text{-PbO-Al}_2\text{O}_3$  system. *J. Non-Cryst Solids.* 1971;5:415–25.
31. Börger A, Supancic P, Danzer R. The ball on three balls test for strength testing of brittle discs: stress distribution in the disc. *J Eur Ceram Soc.* 2002;22:1425–36.
32. Quinn GD. NIST recommended practice guide: fractography of ceramics and glasses. 3rd ed. Gaithersburg, MD: National Institute of Standards and Technology; 2016.
33. Niihara K, Morena R, Hasselman DPH. Evaluation of KIC of brittle solids by the indentation method with low crack-to-indent ratios. *J Mater Sci Lett.* 1982;1:13–6.
34. Hsueh CH, Becher PF. Residual thermal stresses in ceramic composites. Part I: With ellipsoidal inclusions. *Mater Sci Eng A.* 1996;212:22–8.
35. Selsing J. Internal stresses in ceramics. *J Am Ceram Soc.* 1961;44:419.
36. Serbena FC, Zanotto ED. Internal residual stresses in glass-ceramics: a review. *J Non-Cryst Solids.* 2012;358:975–84.
37. Santos GG, Serbena FC, Fokin VM, Zanotto ED. Microstructure and mechanical properties of nucleant-free  $\text{Li}_2\text{O-CaO-SiO}_2$  glass-ceramics. *Acta Mater.* 2017;130:347–60.
38. Villas-Boas MOC, Serbena FC, Soares VO, Mathias I, Zanotto ED. Residual stress effect on the fracture toughness of lithium disilicate glass-ceramics. *J Am Ceram Soc.* 2020;103:465–79.
39. Sabino SRF, Cordeiro BGB, Silva LD, Pukasiewicz AGM, Zanotto ED, Serbena FC. Microstructural and residual stress effects on toughening of stoichiometric  $\text{BaO.2SiO}_2$  glass-ceramics. *J Eur Ceram Soc.* 2022;42:6119–34.
40. West JK, Hench LL. Silica fracture: Part II A ring opening model via hydrolysis. *J Mat Sci.* 1994;29:5808–16.
41. Soga N. Elastic moduli and fracture toughness of glass. *J Non-Cryst Solids.* 1985;73:305–13.
42. Fabris DCN, Miguel EH, Vargas R, Canto RB, Villas-Boas MOC, Peitl O, et al. Microstructure, residual stresses, and mechanical performance of surface crystallized translucent glass-ceramics. *J Eur Ceram Soc.* 2022;42:4631–42.
43. Cook RF, Pharr GM. Direct observation and analysis of indentation cracking in glasses and ceramics. *J Am Ceram Soc.* 1990;73:787–817.
44. Konijnendijk WL, Verweij H. Structural aspects of vitreous  $\text{PbO.2B}_2\text{O}_3$  studied by Raman scattering. *J Am Ceram Soc.* 1976;59:459–61.



45. Shinkai N, Ishikawa H. Crack-branching of binary PbO-B<sub>2</sub>O<sub>3</sub>. *J Non-Cryst Solids*. 1982;52:385–94.
46. Mecholsky JJ, Drexhage MG. Comparison of optical and fractographic measurements of residual stress in compressively clad glass rods. *J Am Ceram Soc*. 1980;63:347–9.
47. Mecholsky JJ, Rice RW, Freiman SW. Prediction of fracture energy and flaw size in glasses from measurements of mirror size. *J Am Ceram Soc*. 1974;57:440–3.

**How to cite this article:** Santos GG, Peitl O, Koike A, Akiba S, Sawamura S, Nagano M, et al. Residual stress versus microstructural effects on the strength and toughness of phase-separated PbO-B<sub>2</sub>O<sub>3</sub>-Al<sub>2</sub>O<sub>3</sub> glasses. *J Am Ceram Soc*. 2023;106:596–612. <https://doi.org/10.1111/jace.18752>